PNAS RESEARCH ARTICLE | PHYSICS

Logarithmic kinetics and bundling in random packings of elongated 3D physical links

Ivan Bonamassa[a,1], Balázs Ráth[b,c,1], Márton Pósfai[a], Miklós Abért[b], Dániel Keliger[b,c], Balázs Szegedy[b], János Kertész[a], László Lovász[b], and Albert-László Barabási[a,d,2]

Affiliations are included on p. 6.

Contributed by Albert-László Barabási; received December 28, 2024; accepted June 16, 2025; reviewed by Antonio Coniglio, Hernan A. Makse, and Gang Yan

We explore the impact of excluded volume interactions on the local assembly of linear physical networks, where nodes are spheres and links are rigid cylinders with varying length. To focus on the effect of elongated links, we introduce a minimal 3D model that helps us zoom into confined regions of these networks whose distant parts are sequentially connected by the random deposition of physical links with a very large aspect ratio. We show that the nonequilibrium kinetics at which these elongated links, or spaghetti, adhere to the available volume without mutual crossings is logarithmic in time, as opposed to the algebraic growth in lower dimensions for needle-like packings. We attribute this qualitatively different behavior to a delay in the activation of depletion forces caused by the 3D nature of the problem. Equally important, we find that this slow kinetics is metastable, allowing us to analytically predict the kinetic scaling characterizing an algebraic growth due to the nucleation of local bundles. Our findings offer a theoretical benchmark to study the local assembly of physical networks, with implications for the modeling of nest-like packings far from equilibrium.

physical networks | nonequilibrium kinetics | bird-nest materials | random packings

Physical networks (1, 2), like brain connectomes (3–6), metamaterials (7–9) or biopolymers (10–12), often display locally ordered structures (13, 14), such as bundles (15–19), where nodes and links are orderly packed together without crossing. While recent studies (20–22) have shed light on the role of volume exclusion in the global structure of such networks, its impact at finer scales remains unknown.

Here, we address this problem by studying the local assembly of linear physical networks (LPNs) (20), a generalization of the Erdős–Rényi model of random graphs where links are rigid cylinders. To zoom into LNPs' confined regions of available space, whose distant parts can be connected by very elongated links, we introduce a minimal bipartite model where links have diameter λ and their endpoints are constrained to the opposite faces of a unitary cube (Fig. 1). As in LPNs, we add links by random sequential deposition (RSD) (23–25) and solve the resulting dynamics analytically, enabling an exact comparison against simulations. We find that at the temporal onset of physicality, $\tau_p \propto 1/\lambda$, the nonequilibrium kinetics of link adhesion undergoes a transition from a noninteracting regime of linear growth to a strongly interacting one where the density of links evolves logarithmically in time, in stark contrast with the algebraic behavior observed in lower dimensions (26–28). We attribute this slow growth to a long–lived balance between rejections, caused by the strong elongation of the links, and depositions, granted instead by the 3D nature of the model. We further demonstrate the metastable nature of the logarithmic regime, which persists until a second time scale, $\tau_b \propto 1/\lambda^{\beta}$ with $\beta \geq 3/2$. This marks the onset of depletion (29–33), accompanied by the formation of local bundles and an algebraic growth $\propto t^{\mu}$, where $\mu^{-1} = 2 + \theta$ and $\theta \in \mathbb{R}^{+}$ is a numerical constant. We validate our predictions by simulations and discuss how these phenomena depend on boundary conditions.

Model

Fig. 1*A* shows a link of diameter λ connecting the opposite faces of a unit cube, modeling a local region of available space in a LPN. Its deposition is performed by selecting uniformly at random its lower endpoint $\mathbf{x} = (x, y) \in [0, 1]^2$ and, independently from $\mathbf{x}$, an angle $\varphi \in [0, 2\pi)$ such that the top endpoint of the link is $\mathbf{x}' = \mathbf{x} + \mathbf{v}_r(\varphi)$, where $\mathbf{v}_r(\varphi) \equiv (r\cos\varphi, r\sin\varphi)$. We assume $r \in (0, 1)$ fixed and $r \gg \lambda$, so that the

Significance

The microstructure of physical networks, where 3D nodes and links obey volume exclusion, is key to understanding their function. Here, we develop a simple model of physical links randomly connecting the opposite faces of a confined box, thanks to which we reveal the emergence of locally ordered structures as the packing densifies. We find that the 3D nature of the problem slows down the growth of the packing to a mean-field logarithmic rate, unlike the faster algebraic behavior in lower dimensions. By computing analytically and numerically characteristic time scales and kinetic exponents, our work not only advances the understanding of physical networks theory but further reveals key results for the nonequilibrium assembly of elongated particles in the experimentally relevant case of 3D systems.

Competing interest statement: A.-L.B. is the funder of Scipher Medicine and owns founder stocks. That company's focus (biotechnology) has no relationship to the topic of this paper (physical networks), so I do not consider it to create conflict. Co-author A.-L.B. and reviewer H.M. were co-authors on a 2023 perspective.

[1]I.B. and B.R. contributed equally to this work.

[2]To whom correspondence may be addressed. Email: barabasi@gmail.com.

This article contains supporting information online at https://www.pnas.org/lookup/suppl/doi:10.1073/pnas.2427145122/-/DCSupplemental.

Published August 4, 2025.

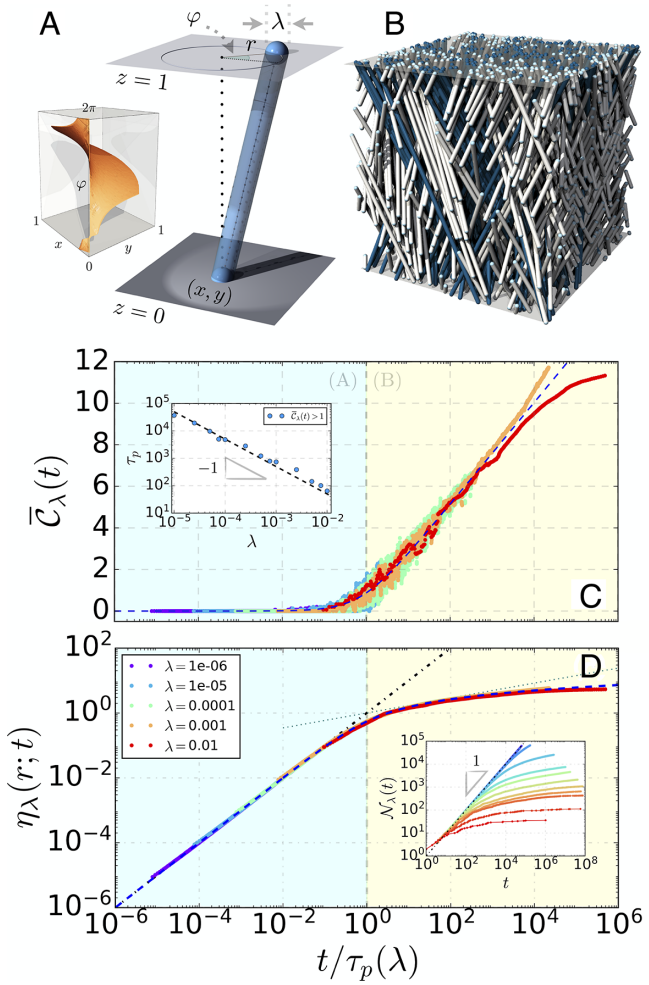

Fig. 1. Packing bipartite nests. (*A*) Randomly deposited link with thickness λ, projection length r, and a randomly selected angle $\varphi \in [0, 2\pi)$. (*Inset*) Configurations excluded by the deposition of a single link with $\lambda = 1/500$ and $r = 1/2$. (*B*) Nearly saturated configuration of $\mathcal{N}_\lambda = 432$ links with $\lambda = 1/50$, $r = 1/2$, and horizontally periodic boundary conditions (PBCs). Blue and white colors distinguish links falling within the bulk of the cube from those puncturing its walls (azure caps) and reemerging at the opposite face. (*C*) Average number of conflicts, $\bar{\mathcal{C}}_\lambda$, experienced by virtual links between valid depositions for $r = 1/2$. For the colors of the curves and regions, see the legend in (*D*). The dashed curve corresponds to the analytical solution, Eq. **2**, while $t = \tau_p(r;\lambda)$ marks the onset of physicality. (*Inset*) Numerical timescales (symbols) vs. analytical prediction $\tau_p = \pi/2\lambda$ (dashed line). (*D*) Evolution of the rescaled number of deposited links, $\eta_\lambda(r;t)$; notice the linear regime (black dot-dashed line) and the analytical solution (blue dashed curve), Eq. **2**. The dotted line reflects the asymptotic scaling in Eq. **4**. *Left* (light blue): (*A*) nonphysical regime; *Right* (light yellow): (*B*) physical regime. (*Inset*) Raw evolution of $\mathcal{N}_\lambda(t)$ for increasing (violet-to-red) values of λ highlighting the linear growth in the nonphysical regime. In simulations, we deposit links with diameter λ until either $\mathcal{N}_\lambda = 10^5$ or $t \geq 10^9$; in the latter case, we consider the packing saturated.

relevant length of each link greatly exceeds its thickness; in practice, this corresponds to aspect ratios $r/\lambda \gtrsim \mathcal{O}(10^2)$, consistent with the typical range of values adopted e.g. in fiber networks (8) and observed in bird-nest materials (11). We study the model under periodic boundary conditions (PBCs, Fig. 1*B*) and address boundary effects later on.

Link deposition proceeds by iterating two steps: *i*) a virtual link is generated following the above protocol; it is then tested for collisions with the previously deposited links and, where present, with the box's boundaries; *ii*) if no collision is detected, the virtual link is deposited, otherwise it is rejected. Like in LPNs (20) and other RSD kinetics (24), a saturated or jammed state is reached when no more links can be formed due to volume exclusion (Fig. 1 *A*, *Inset*). In the deposition of elongated 3D links, however, this asymptotic regime is preceded by an intermediate one during which the rejection of links is insensitive to their volume, $\mathcal{O}(\lambda^2)$, depending instead on the links' diameter, λ. In fact, since links are sampled uniformly at random, the probability that one of them has no conflict with n previously deposited links is $\pi_0 \approx (1-p)^n$, where p is the probability that two randomly chosen links intersect. We have $p = m_r\lambda$, where $m_r = 4r/\pi$ is the expected Euclidean length of the difference of two random vectors with length r and a uniformly distributed angle. Note that if $n \ll 1/p$ then $\pi_0 \approx 1$, but if $n \gg 1/p$ then $\pi_0 \approx 0$. Thus, denoting with t the number of attempted depositions and $\mathcal{N}_\lambda(t)$ the number of deposited links at time t, we have $\mathcal{N}_\lambda(t) \approx t$ if $t \ll 1/p$ and $\mathcal{N}_\lambda(t) \ll t$ if $t \gg 1/p$. In other words, the characteristic time scale $\tau_p = 1/m_r\lambda$ marks the onset of physicality above which at least one virtual link is rejected with finite probability before a successful deposition. Fig. 1*C* shows the evolution of the average number of conflicts, $\bar{\mathcal{C}}_\lambda$, experienced by virtual links between valid depositions. As visible, $\bar{\mathcal{C}}_\lambda$ undergoes a transition above τ_p from a nonphysical regime (region A in Fig. 1*C*), where links behave as if they had vanishing thickness, to a physical one (region B), characterized by a large number of conflicts.

To understand the kinetics of the model, we develop a continuous-time approximation (*SI Appendix*, sections S.1–S.3) for the growth rate of $\mathcal{N}_\lambda(s)$ with $s \equiv t/\tau_p$. This leads to a Langmuir-type equation $\frac{\mathrm{d}\mathcal{N}_\lambda}{\mathrm{d}s} = \tau_p\Psi[r;\mathcal{N}_\lambda(s)]$, where $\Psi[r;\mathcal{N}_\lambda(s)]$—the volume fraction eligible for a new link—corresponds to the probability of a successful deposition at time s. Evaluating Ψ requires characterizing the random geometry of the accessible configurations, a highly nontrivial task due to the overlap of excluded volumes from previously deposited links (Fig. 1 *A*, *Inset*). To enable analytical progress, we adopt a meanfield approximation and assume that the link's excluded volumes are additive, i.e. their mutual overlaps can be neglected. Under this assumption, the decay of $\Psi[r;\mathcal{N}_\lambda(s)]$ can be described as a Poisson thinning process, so that $\Psi = [1-\lambda m_r]^{\mathcal{N}_\lambda(s)} \simeq \exp\{-\lambda m_r \mathcal{N}_\lambda(s)\}$, which yields

$$\frac{\mathrm{d}\mathcal{N}_\lambda(s)}{\mathrm{d}s} = \tau_p e^{-\lambda m_r \mathcal{N}_\lambda(s)}, \quad \mathcal{N}_\lambda(0) = 0, \qquad [1]$$

whose solution predicts the logarithmic growth

$$\eta_\lambda(r;t) = \ln\left(1 + \frac{t}{\tau_p(r;\lambda)}\right), \qquad [2]$$

where $\eta_\lambda(r;t) \equiv \lambda m_r \mathcal{N}_\lambda(r;t)$. The kinetics in Eq. **2** is markedly slower when compared to the algebraic growth (see Table 1 in *Discussion*) characterizing RSD of $d = 1, 2$ elongated needles (26–28). We attribute the slow growth above τ_p to an interplay between two competing mechanisms: While the elongation of links depletes a large fraction of possible configurations (*Inset*, Fig. 1*A* and *SI Appendix*, Fig. S1)—like in $d \leq 2$ needle-packings (*SI Appendix*, Fig. S2)—the 3D nature of the problem grants sufficient spatial freedom to mitigate the effect of excluded volume overlap, allowing many nearly independent depositions. This yields a long-lived balance between rejections and acceptances of the links, demonstrated by the identical evolutions of $\mathcal{C}_\lambda$ and $\mathcal{N}_\lambda$ in Fig. 1 *C* and *D*, that delays depletion-induced correlations, needed for the emergence of local order. In *Discussion*, we elaborate further on the generality of this phenomenon and its relation to RSD kinetics in other dimensions.

Kinetic Instability

Simulated link packings (Fig. 1*B*) closely follow the evolution predicted by Eq. **2** for several orders of magnitude and for a broad range of link diameters λ (details in caption, Fig. 1*B* and *SI Appendix*, Fig. S3). Yet, a closer inspection of the difference, $\mathcal{D}_\lambda(t)$, between simulations and Eq. **2** reveals the emergence of instabilities at times much above τ_p which, as we show below, are due to the activation of depletion effects and the formation of local link bundles.

We start by analyzing the influence of different aspect ratios r/λ on $\mathcal{D}_\lambda(t)$. As shown in Fig. 2, packings corresponding to $r \in \{1/4, 1/2, 3/4\}$ undergo systematic deviations from Eq. **2** above τ_p. While negative deviations correspond to packings undergoing saturation—which we define by setting a maximum waiting time $t = 10^9$ between successful depositions—the positive overswing of $\mathcal{D}_\lambda(t)$ (Fig. 2 *B*, *E*, and *H*) at large aspect ratios indicates instead a faster deposition rate compared to the logarithmic prediction. Beginning from $r = 1/4$ (Fig. 2*A*), we find that these positive deviations occur if $r/\lambda \gtrsim \mathcal{O}(10^2)$ and their extent widens for large r. This is evident, e.g., in the evolution of the difference $\mathcal{D}_\lambda$ corresponding to links of diameter $\lambda = 10^{-2}$ in Fig. 2 *B*, *E*, and *H* (see also *SI Appendix*, Figs. S3 and S4 for results with $r = 1$).

To understand this phenomenon, recall that the exponential decay of the deposition probability Ψ—lying at the heart of the logarithmic growth, Eq. **2**—assumes that collisions of virtual links are independent and identically distributed. This hypothesis breaks down above τ_p, at which the virtual collisions promote newly deposited links to align with the existing configuration, favoring the formation of link bundles. This implies the emergence of privileged directions of deposition, potentially reflected in inhomogeneities of the link's angle distribution with respect to the uniform background. In Fig. 2 *C*, *F*, and *I*, we test this hypothesis by analyzing the evolution of detrended fluctuations of the links' angle distribution, $\mathcal{F}(\varphi/2\pi; t)$ (details in caption, Fig. 2). The snapshots taken from the onset of physicality (black symbols) until the last deposition (teal symbols, Fig. 2—see also *SI Appendix*, Figs. S3 and S4), indicate that the instabilities reported in Fig. 2 *B*, *E*, and *H* correspond to structured inhomogeneities of the link's angle distribution, having sinusoidal shape and self-amplifying over time.

Analytical insights about this empirical observation can be found by mimicking the spontaneous formation and growth of a bump in the links' angle distribution from a planted inhomogeneous configuration. In this case Eq. **1** can be rewritten as (*SI Appendix*, section S.5)

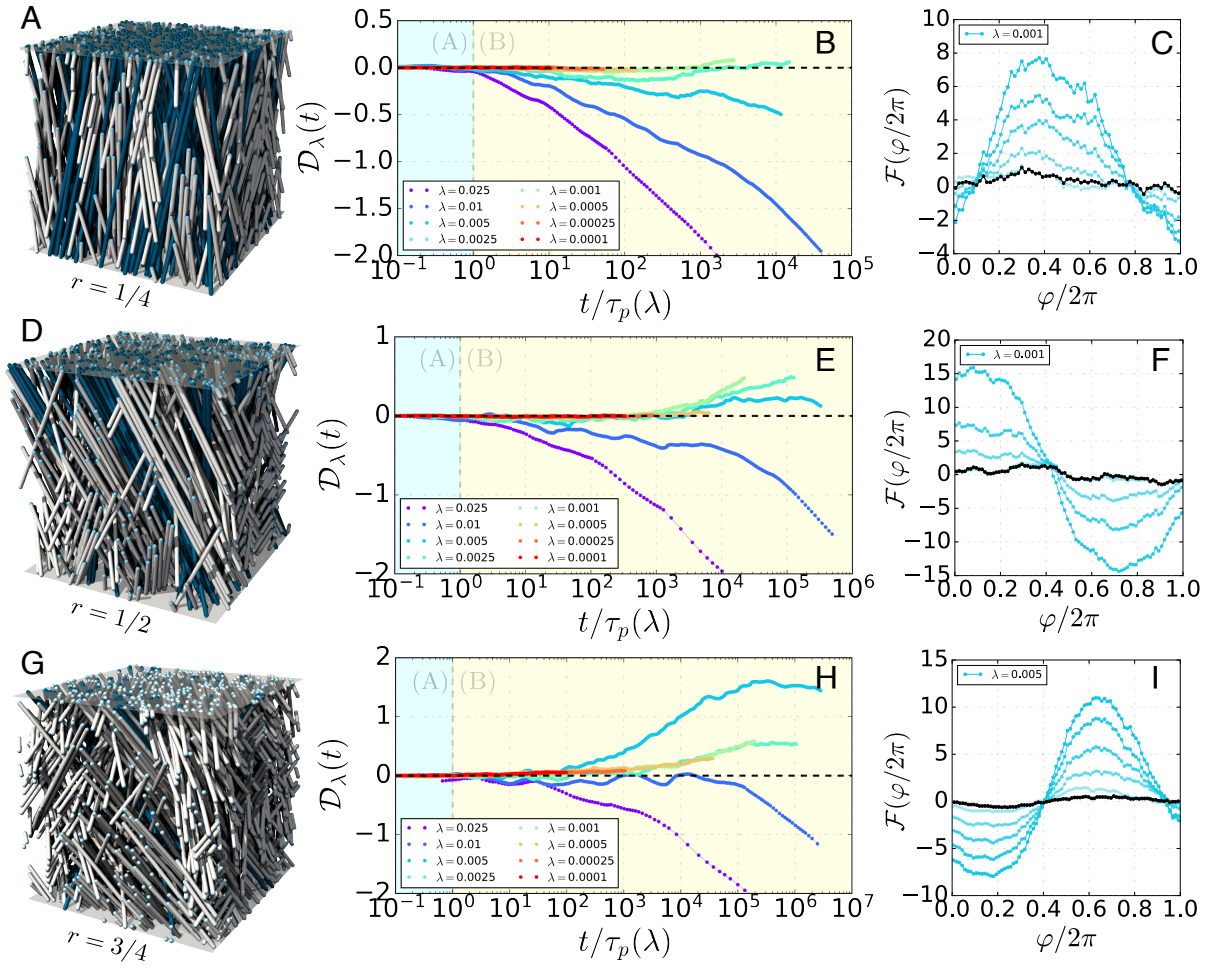

Fig. 2. Kinetic instabilities. (*A*) Nearly saturated packing of links with $r = 1/4$ and $\lambda = 1/10$. (*B*) Temporal evolution of the difference, $\mathcal{D}_\lambda(t)$, between simulations and theoretical prediction, Eq. **2**. Light blue (*A*) and light yellow (*B*) regions are defined as in Fig. 1 *C* and *D*. (*C*) Stroboscopic snapshots of the fluctuations, $\mathcal{F}(\varphi/2\pi)$, obtained by detrending the empirical links' angular distribution of the uniform background expected at deposition times $T = n\tau_p$, with $n = 1, 2, 3\ldots$. Visibly, a sinusoidal inhomogeneity (teal symbols) amplifies over time (increasing opacity) out of the uniform trend above the onset of physicality τ_p (black symbols). (*D–F*) and (*G–I*) show results as in (*A–C*) for $r = 1/2$ and $r = 3/4$, respectively.

$$\dot{r}(t,\varphi) = \exp\left(-\frac{1}{2\pi}\int_0^{2\pi} r(t,\varphi^*)\,\|\mathcal{A}_r(\varphi,\varphi^*)\|\,\mathrm{d}\varphi^*\right), \quad [3]$$

where $\mathcal{A}_r(\varphi,\varphi^*) \equiv \mathbf{v}_r(\varphi) - \mathbf{v}_r(\varphi^*)$ and $r(t,\varphi)$ is a function such that $\mathcal{N}_\lambda(t) \simeq \frac{1}{\lambda}(\int_0^{2\pi} r(t,\varphi)\mathrm{d}\varphi - \mathcal{N}_\star)$, with $\mathcal{N}_\star$ being the number of initial links deposited unevenly. We note that, if $\mathcal{N}_\star = 0$, the linearization of Eq. **3** around Eq. **2** yields sinusoidal eigenfunctions. For $\mathcal{N}_\star \neq 0$, we search instead for a self-similar solution of Eq. **3** with the factorized form $r(t,\varphi) \approx h^2(t)\hat{r}(\varphi h(t))$ at large t, where $\hat{r} : \mathbb{R} \to \mathbb{R}^+$ models the shape of the inhomogeneity and $h : \mathbb{R}^+ \to \mathbb{R}^+$ governs its temporal evolution. Ultimately, we find that for $t \gg \tau_p$

$$\mathcal{N}_\lambda(t) \propto \alpha_\lambda\, t^\mu, \quad \mu \equiv (2+\theta)^{-1}, \quad [4]$$

where $\alpha_\lambda \equiv \lambda^{-(1+\theta)/(2+\theta)}$ and $\theta \simeq 2.3389\ldots$ is an integral constant (*SI Appendix*, Eq. S20). Eq. Eq. **4** shows that Eq. **2** is an unstable solution of Eq. **1** to random fluctuations of the links' angle distribution, whose nucleation speeds up the kinetics in algebraic fashion.

While suggestive, large coherent inhomogeneities like those assumed above unlikely form spontaneously, hindering the global behavior predicted by Eq. **4**. This is visible in Fig. 1*D* (*SI Appendix*, Fig. S3), where the scaling in Eq. **4** is displayed (dotted line) for comparison.

Bundle Formation

The algebraic growth in Eq. **4** can be observed by studying locally the formation of bundles. First, note that the self-similar solution of Eq. **3** indicates that, as more links are deposited, they become increasingly aligned. In fact, the expected angle between randomly chosen links evolves as $\vartheta(t) \propto \ln(h(t))/h(t)$, where $h(t) \propto t^\mu$ for $t \gg \tau_p$ (*SI Appendix*). Hence, the orientational correlation function $g(t) := 1 - \langle\cos\vartheta\rangle$ decays algebraically with a logarithmic prefactor as $g(t) \propto t^{-\mu}\ln t$, where μ is the scaling exponent defined in Eq. **4**.

While the above confirms that links become asymptotically parallel, it does not bear information about their positional order. Because this analysis gets mathematically demanding, we characterize local bundle formation via simulations. To compute the latter, we identify the set of nearest neighbors of a link in the top and bottom plane using a proximity graph (details in *SI Appendix*, section S.6) constructed via the 2*D* α-complex of the links' coordinates (35). We then consider two physical links as bundled if they are nearest neighbors in both the bottom and the top plane of the unit box. We measure the bundling number, $\mathcal{B}_\lambda(t)$, representing the total number of bundled links divided by its corresponding value in the nonphysical limit ($\lambda = 0$) which is proportional to $\sqrt{\mathcal{N}_0}$ (*SI Appendix*, section S.6). We also quantify the relative orientation of link bundles by their local nematicity $\mathcal{O}_i = \sum_{j\in\partial i} P_2(\varphi_{ij})/k_i$, where P_2 is the second Legendre polynomial, $\varphi_{ij} = \varphi_i - \varphi_j$ is the relative angle between links i and j, and k_i is the degree of the i-th physical link in the proximity graph.

Fig. 3 *A* and *B* highlight the bundles formed until the last deposition, indicating that locally aligned links typically form pairs and small motifs. Interestingly, a similar pairing phenomenon has been observed in the self-limited assembly of nanorods (18) in the presence of attractive van der Waals forces. In our model, instead, these microstructures spontaneously nucleate under the sole effect of volume exclusion from local fluctuations of the links' angle distribution, whose growth can be interpreted as a local analogue of the self-amplifying mechanism underlying Eq. **3**, suggesting an algebraic growth akin to Eq. **4**. Fig. 3*C* supports this rationale (Fig. 4 *C* and *G*), whose agreement with simulations increases at larger aspect ratios (*SI Appendix*, Fig. S7). The *Inset* of Fig. 3*C* confirms that bundled links are nearly parallel.

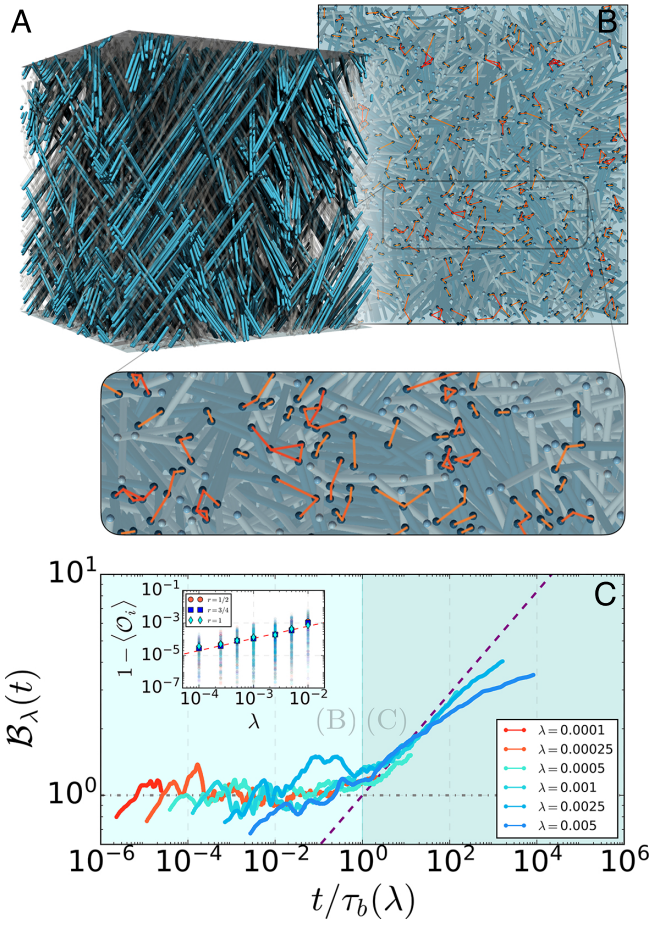

Fig. 3. Local bundling. (*A*) Configuration of bundles, highlighted in color out of a nearly saturated packing of 3D links with $r = 1/2$ and $\lambda = 1/100$. (*B*) *Bottom* plane view, displaying bundled links (in blue) identified by positional proximity (orange bonds) and their assembly in small microstructures (zoom-out *Inset*). (*C*) Evolution of the bundling number, $\mathcal{B}_\lambda(t)$ of the packing; notice the onset of bundling $\tau_b(\lambda) \propto \lambda^{-\beta}$ with $\beta \simeq 1.75$—marking the kinetic transition from the physicality regime (*B*) to the bundling regime (*C*)—and the algebraic growth, Eq. **4**, above τ_b (dashed line). See also *SI Appendix*, Fig. S7 for results with $r = \{3/4, 1\}$. (*Inset*) Local nematicity, $\mathcal{O}_i$, of bundled links and their average (symbols) for $r \in \{1/2, 3/4, 1\}$; notice the power-law decay $\langle\mathcal{O}_i\rangle \sim 1 - \lambda^{-3/4}$ (red dashed line).

Depletion Activation

In Fig. 3*C* and *SI Appendix*, Fig. S7 *C* and *F*, we have rescaled the bundling number in units of a new time scale $\tau_b \propto \lambda^{-\beta}$, whose exponent $\beta > 1$ indicates that ordered microstructures emerge always above the onset of physicality. We support this observation by studying the stability of a planted inhomogeneity above τ_p. In essence (details in *SI Appendix*, section S.7), we consider the space–dependent Langmuir–type equation for the bipartite model, i.e. $\partial_\tau\rho(\mathbf{x},\varphi,\tau) = \exp\{-(\mathcal{A}\rho)(\mathbf{x},\varphi,\tau)\}$, where $\mathcal{A}$ is a (self-adjoint) integral operator (*SI Appendix*, Eq. **S4** and section S.2) and $\tau \equiv t/\tau_p(r;\lambda)$ is the rescaled time in Eq. **2**. We linearize around the constant function $\rho(\mathbf{x},\varphi,t) \equiv \rho(t)$ which solves $\partial_\tau\rho = e^{-\gamma\rho}$—i.e. the logarithmic growth, Eq. **2**—

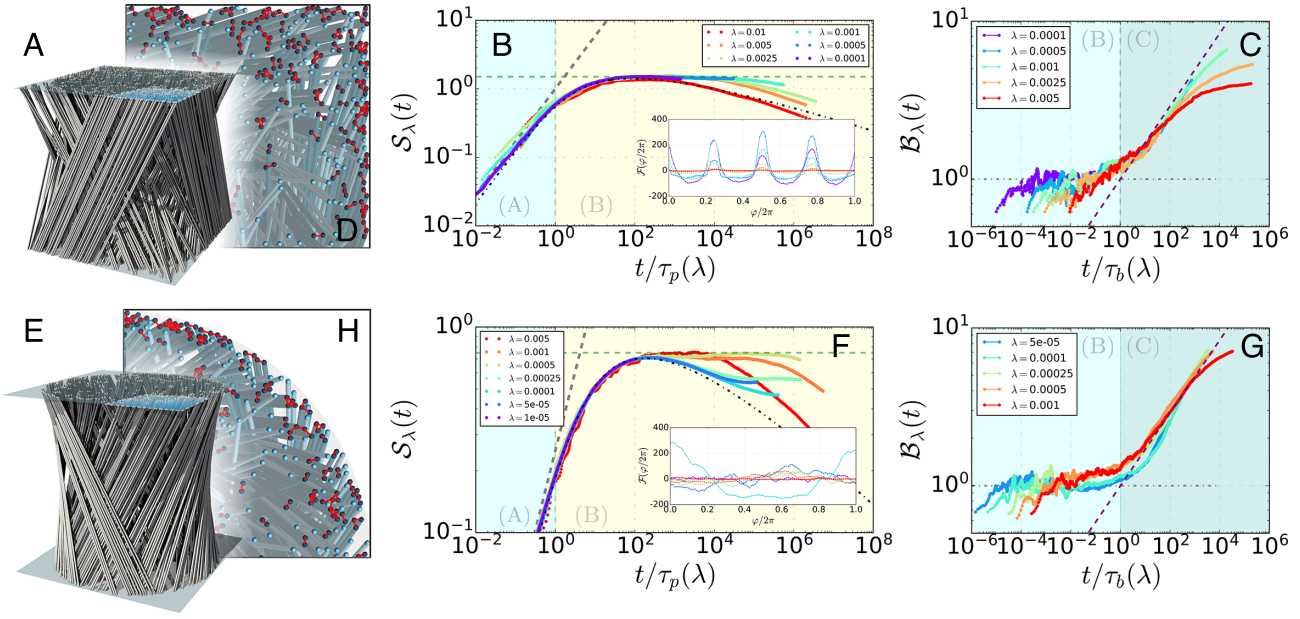

Fig. 4. Growth and bundling in the bipartite model with given boundary shapes. (*A*) Nearly saturated packing of bipartite spaghetti with diameter $\lambda = 1/100$ and projection length $r = 1/2$ in a unitary cube. Notice the strong alignment in proximity of the hard boundaries. (*B*) Rescaled link density, $\mathcal{S}_\lambda(t) \equiv \rho_\lambda(t)/t^\mu$ with $\mu^{-1} = 2 + \theta$ and $\theta = 2.3389\ldots$, highlighting a macroscopic regime of algebraic growth defined by the asymptotic scaling in Eq. **4** (teal dashed line). Colored regions are defined as in Fig. 1 *C* and *D*. Like in Fig. 1*D*, the black dot-dashed curve highlights the logarithmic growth in Eq. Eq. **2**. (*Inset*) Angular distribution at saturation, displaying large inhomogeneities caused by the box hard-walls. (*C*) Evolution of the bundling number, $\mathcal{B}(t)$, characterizing the formation of motifs of bundled spaghetti, marked in (*D*) by red bonds in the zoomed portion of the *Top* plane of the box highlighted in blue in (*A*); similarly to the case of periodic boundary conditions, also here the onset of bundling, τ_b, is decoupled from the onset of physicality, τ_p, with $\tau_b(\lambda) \propto \lambda^{-\beta}$ with $\beta \simeq 1.5$. (*E*) Nearly saturated packing of bipartite rods with $\lambda = 1/100$ and $r = 1/2$ constrained to a cylindrical box of unitary height and diameter; notice the formation of shells of oriented spaghetti. Figures (*F–H*) follow the same captions as for the cubic box model, with the difference that the onset of bundling, $\tau_b(\lambda)$ scales now as $\tau_b(\lambda) \propto \lambda^{-\beta}$ with $\beta \simeq 1.8$ (see text for more details).

where $\mathcal{A}\mathbb{1} =: \gamma\mathbb{1}$ and $\gamma \in \mathbb{R}^+$ is the leading eigenvalue of $\mathcal{A}$ and $\mathbb{1}$ is the indicator operator of a successful deposition. The perturbation $\tilde{\rho} = \rho + \xi$ yields $\partial_\tau \xi = \exp\{-\gamma\rho\}(\exp\{-\mathcal{A}\xi\} - 1)$ which, to leading orders, can be written in linear form $\partial_\tau \xi = -(\gamma\tau + 2\pi)^{-1}\mathcal{A}\xi$. We search for solutions with the factorized form $\xi(\mathbf{x}, \varphi, \tau) = \mathcal{C}(\tau)\psi(\mathbf{x}, \varphi)$, where $\psi : [0, 1]^2 \times [0, 2\pi) \to \mathbb{R}$ is such that $(\mathcal{A}\psi)(\mathbf{x}, \varphi) = \mu\psi(\mathbf{x}, \varphi)$ and μ is the most negative eigenvalue of $\mathcal{A}$; notice that $-\infty < \mu < 0$ since $\mathcal{A}$ has zero trace. The temporal profile, $\mathcal{C}(\tau)$, then solves $\partial_\tau \ln \mathcal{C} = -\mu(\gamma\tau + 2\pi)^{-1}$, yielding the scaling $\mathcal{C}(\tau) \simeq \mathcal{C}(1)\tau^{-\mu/\gamma}$, where $|\mu|/\gamma \in (0, 1)$ and $C(1) \simeq \sqrt{\lambda}$ (see *SI Appendix*, section S.7 for details). Summing up the above, we find $\tilde{\rho} \simeq \rho + \sqrt{\lambda}\tau^{-\mu/\gamma}\psi$ so that, to leading orders, a global inhomogeneity emerges as soon as $C(\tau) > 1$, that is roughly above a second characteristic time scale

$$\tau_b(\lambda) \propto \lambda^{-\beta}, \quad \beta \equiv 1 + \frac{\gamma}{2|\mu|}. \qquad [5]$$

Since $\gamma/|\mu| \geq 1$, it follows that $\beta' = 3/2$ is a lower bound for the onset of depletion, in agreement with the characteristic time scales observed in Fig. 3*C* and *SI Appendix*, Fig. S7 *C* and *F*. Notice that, owing to their distinct λ dependencies, the separation between τ_p and τ_b increases as the link thickness decreases, thereby delaying the onset of orientational order in packings of progressively thinner physical links.

Boundary Effects

We now explore the influence of hard boundaries on the kinetics of our model. In particular, we analyze the cases of cubic and cylindrical shapes of the box where the spaghetti are sequentially deposited. Although we do not solve analytically these cases, we expect to observe kinetics regimes akin to those reported in the model under PBCs. The intuition behind this roots on Rényi's car parking problem in one dimension (36, 37), where inhomogeneities in density and order correlations in RSD develop in a similar way, whether particles interact with each other or with the boundaries of the interval. In 3D, on the other hand, we expect that the presence of extended boundaries will boost the activation of depletion forces with respect to the case with PBCs, attracting spaghetti to the walls (33, 38). Hence, we anticipate that microconfigurations of bundled spaghetti will form earlier than in the case with PBCs and that the packing kinetics will rapidly escape the metastable regime of logarithmic growth.

We start from cubic hard boundaries. Fig. 4*A* shows a nearly saturated packing of elongated spaghetti deposited within a unit cube. As visible, large bundles of physical links form oriented structures near the external faces of the box and, as expected, the evolution of the spaghetti density departs from logarithmic growth earlier than in the model with PBCs. To highlight the latter, we plot in Fig. 4*B* the rescaled link density, $\mathcal{S}_\lambda(t) \equiv \rho_\lambda(t)/t^\mu$ with $\mu^{-1} = 2 + \theta$ and $\theta = 2.3389\ldots$, which reveals a long-lived regime of algebraic growth, with the same kinetic scaling predicted by Eq. **4**. Notice that this is in contrast with the kinetics found in the model with PBCs, where the scaling law in Eq. **4** could not be observed during the evolution of the packing's density (see *SI Appendix*, Fig. S3 and results therein). The appearance of the kinetic exponent $\mu^{-1} = 2 + \theta$ in the presence of hard boundaries can be explained by noticing that the planted inhomogeneities assumed in the self-similar argument leading to the algebraic growth in Eq. **4** in the case with PBCs (*SI Appendix*, section S.5) naturally arise here due to the privileged orientations imposed by the box's hard boundaries, which are visible in the *Inset* to Fig. 4*B*. These effects

favor the formation of bundles close to the boundaries, as shown in Fig. 4*D*, whose intensity is measured by the bundling number, $\mathcal{B}_\lambda(t)$. The evolution of $\mathcal{B}_\lambda(t)$ (Fig. 4*C*) reaches values nearly 10 times larger then the nonphysical reference, $\mathcal{B}_0(t) \sim \sqrt{t}$ (c.f. with the $r = 1/2$ case with PBCs studied in the main text). Furthermore, as expected, we show numerically that the onset of bundling, τ_b, is still decoupled from the onset of physicality, τ_p and scales as $\tau_b(\lambda) \propto \lambda^{-\beta}$ with $\beta \simeq 1.5$, i.e. at an earlier time scale then in the case with PBCs.

In the case of a cylindrical box, shown in Fig. 4*E*, we find a richer scenario. Here, the hard cylindrical boundaries still attract the deposition of spaghetti while leaving more freedom in their orientation. It is visible from the saturated packing shown in Fig. 4*E* that spaghetti self-assemble in chiral shells around the cylinder's disk, forming surfaces characterized by locally aligned particles with clockwise or counterclockwise orientations (Fig. 4*H*). Similarly to the case of the cubic box, also here (Fig. 4*F*) the link density exhibits a regime of algebraic growth characterized by the scaling in Eq. **4** whose duration lasts for several orders of magnitudes. However, differently from the cubic box case, the angle distribution (Fig. 4*F*) of nearly saturated packings does not reveal clear patterns of inhomogeneities, suggesting that spatial correlations play a major role in this setting. Surprisingly, despite these intriguing differences, the growth of spaghetti bundles is, here as well, in good agreement with the analytical algebraic scaling, Eq. **4**, found for the model with PBCs and observed in the case of hard cubic boundaries.

Discussion

We have studied a minimal 3D model characterizing the local assembly of links in linear physical networks (20) and showed that it features rich kinetics, characterized by long-lived metastable regimes of logarithmic growth, dynamic instabilities, and bundle formation. Remarkably, these phenomena persist in the presence of hard boundaries of varying shape (*SI Appendix*, section S.7) as shown in Fig. 4 for packings in cubic (Fig. 4 *A–D*) and cylindrical boxes (Fig. 4 *E–H*). Despite some intriguing differences—such as the formation of density and orientational inhomogeneities—we attribute these similarities to the strong elongation of the physical links and the 3D nature of the system, whose interplay underlies the long-lived logarithmic kinetics observed. In *SI Appendix*, section S.8, in particular, we show that the logarithmic growth persists for an even longer lifetime (*SI Appendix*, Fig. S8) when relaxing the bipartite constraint of the model.

It is worth emphasizing that mean-field Langmuir-type equation, Eq. **1**, and their logarithmic solutions, Eq. **2**, can in principle describe any RSD kinetics of hard-core particles, from disks to spheres or needles. However, in dimensions $d \leq 2$, the mean-field approximation underlying the independence of the excluded volumes of the particles typically breaks down at the onset of physicality, yielding a kinetic transition from linear (noninteracting) to algebraic growth (24, 25), where local orientational order emerges. Drawing an analogy with critical phenomena—where mean-field approximations improve with increasing dimensionality—logarithmic kinetics become increasingly accurate in describing the growth of elongated particles as dimension grows. This suggests the possibility of an upper critical dimension above which the RSD kinetics of elongated particles are characterized by stable logarithmic growth. Such regime, which in our 3D physical link model is long-lived but metastable to random fluctuations of the links orientation, is therefore a distinct dynamical phase of RSD packings, where growth is curtailed by volume exclusion yet no local orientational order emerges.

Table 1. Kinetic scalings above the onset of physicality and above the onset of bundling (ordering growth), together with the orientation decay and the ordering time scale in RSD packings of elongated needles—i.e. with infinite aspect ratio, α—in $d = 1, 2$ compared with the results of this work for $d = 3$ highly elongated—aspect ratios $r/\lambda \gtrsim \mathcal{O}(10^2)$—physical links

	$d = 1, 2$	$d = 3$
kinetic growth	$\sim t^{1/3}$ (26)	$\sim \ln(1+t)$
ordering growth	$\sim t^{\sqrt{2}-1}$ (28)	$\sim t^{\mu}$
correlations decay	$\sim t^{\sqrt{3}-\sqrt{2}-1}$ (25)	$\sim t^{-\mu} \ln t$
ordering time scale	$\tau' \sim \alpha^{3/(1+2\sqrt{2})}$ (34)	$\tau_b \gtrsim \lambda^{-3/2}$

Notice that, in $d = 3$, the algebraic scaling of ordering growth has exponent $\mu \equiv (2+\theta)^{-1}$ with $\theta \simeq 2.3389\ldots$ (see Eq. **4** for more details). See refs. 24 and 25 for details about the results of $d = 1, 2$ needle-like packings.

We expect this slow growth to be a general phenomenon extending to LPNs made of very elongated links, with potential implications for the modeling of nonequilibrium assembly of "bird-nest" materials (11) and nest-like packings (18, 39). This is an intriguing direction for future research, bearing analogies with glass formers (40–42), relaxation in granular compactions (43, 44) and other kinetically constrained systems (45–47). In this regard, it would be desirable to understand how the onset of saturation depends on the geometry of the random link packings. Furthermore, we expect that generalizations of our null model, obtained by e.g. relaxing the rigidity of the links via curvilinear fibers and/or by enabling equilibration steps e.g. by molecular dynamics (38), will provide fruitful venues for developing mathematically tractable models of physical networks with increasingly realistic features. In this context, we believe our simple model could offer insights about bundle formation in systems like neuronal or vascular networks (48), where elongated structures grow under geometric or excluded volume constraints. Finally, from a theoretical perspective, our results make essential steps forward for the theory of RSD of elongated particles, where analytical solutions are only known in $d = 1$ and $d = 2$ dimensions (Table 1), providing relevant insights for $d = 3$ dimensions, a crucial case for real applications.

Data, Materials, and Software Availability. The data and code used in this study are publicly available at the GitHub repository: https://github.com/hokanoei/Bundling_spaghetti (49).

ACKNOWLEDGMENTS. This research was funded by ERC grant No. 810115-DYNASNET. B.R. acknowledges partial funds from NKFI-FK-142124 of NKFI (National Research, Development and Innovation Office).

Author affiliations: [a]Department of Network and Data Science, Central European University, Vienna 1100, Austria; [b]Hungarian Research Network, Alfréd Rényi Institute of Mathematics, Budapest H-1053, Hungary; [c]Department of Stochastics, Institute of Mathematics, Budapest University of Technology and Economics, Budapest H-1111, Hungary; and [d]Department of Physics, Network Science Institute, Northeastern University, Boston, MA 02215

Author contributions: I.B. performed numerical simulations and analyzed the data; I.B., B.R., and D.K. contributed to analytical calculations; I.B. and A.-L.B. wrote the paper; and I.B., B.R., M.P., M.A., D.K., B.S., J.K., L.L., and A.-L.B. designed and interpreted the research, reviewed and edited the manuscript.

Reviewers: A.C., University of Naples; H.A.M., The City College of New York Benjamin Levich Institute for Physico-Chemical Hydrodynamics; and G.Y., Tongji University.

1. N. Dehmamy, S. Milanlouei, A. L. Barabási, A structural transition in physical networks. *Nature* **563**, 676–680 (2018).
2. Y. Liu, N. Dehmamy, A. L. Barabási, Isotopy and energy of physical networks. *Nat. Phys.* **17**, 216–222 (2021).
3. M. Rivera-Alba *et al*., Wiring economy and volume exclusion determine neuronal placement in the *Drosophila* brain. *Curr. Biol.* **21**, 2000–2005 (2011).
4. E. Bullmore, O. Sporns, The economy of brain network organization. *Nat. Rev. Neurosci.* **13**, 336–349 (2012).
5. M. Winding *et al*., The connectome of an insect brain. *Science* **379**, eadd9330 (2023).
6. X. Y. Zhang, J. M. Moore, X. Ru, G. Yan, Geometric scaling law in real neuronal networks. *Phys. Rev. Lett.* **133**, 138401 (2024).
7. M. Kadic, G. Milton, M. van Hecke, M. Wegener, 3D metamaterials. *Nat. Rev. Phys.* **1**, 198–210 (2019).
8. C. R. Picu, *Network Materials: Structure and Properties* (Cambridge University Press, 2022).
9. M. Zaiser, S. Zapperi, Disordered mechanical metamaterials. *Nat. Rev. Phys.* **5**, 1–10 (2023).
10. P. G. D. Gennes, J. Prost, *The Physics of Liquid Crystals* (Oxford University Press, 1993).
11. N. Weiner, Y. Bhosale, M. Gazzola, H. King, Mechanics of randomly packed filaments–the "bird nest" as meta-material. *J. Appl. Phys.* **127**, 050902 (2020).
12. A. Neophytou, D. Chakrabarti, F. Sciortino, Topological nature of the liquid-liquid phase transition in tetrahedral liquids. *Nat. Phys.* **18**, 1248–1253 (2022).
13. A. Baule, R. Mari, L. Bo, L. Portal, H. A. Makse, Mean-field theory of random close packings of axisymmetric particles. *Nat. Commun.* **4**, 2194 (2013).
14. A. Baule, F. Morone, H. J. Herrmann, H. A. Makse, Edwards statistical mechanics for jammed granular matter. *Rev. Mod. Phys.* **90**, 015006 (2018).
15. N. T. Markov *et al*., Cortical high-density counterstream architectures. *Science* **342**, 1238406 (2013).
16. B. Q. Chandio *et al*., Bundle analytics, a computational framework for investigating the shapes and profiles of brain pathways across populations. *Sci. Rep.* **10**, 1–18 (2020).
17. M. Jasnin *et al*., Three-dimensional architecture of actin filaments in listeria monocytogenes comet tails. *Proc. Natl. Acad. Sci. U.S.A.* **110**, 20521–20526 (2013).
18. G. Jia *et al*., Couples of colloidal semiconductor nanorods formed by self-limited assembly. *Nat. Mater.* **13**, 301–307 (2014).
19. S. Chakraborty, M. Jasnin, W. Baumeister, Three-dimensional organization of the cytoskeleton: A cryo-electron tomography perspective. *Protein Sci.* **29**, 1302–1320 (2020).
20. M. Pósfai *et al*., Impact of physicality on network structure. *Nat. Phys.* **20**, 142 (2024).
21. G. Pete, Á. Timár, S. Ö. Stefánsson, I. Bonamassa, M. Pósfai, Physical networks as network-of-networks. *Nat. Commun.* **15**, 4882 (2024).
22. C. Glover, A. L. Barabási, Measuring entanglement in physical networks. *Phys. Rev. Lett.* **133**, 077401 (2024).
23. J. W. Evans, Random and cooperative sequential adsorption. *Rev. Mod. Phys.* **65**, 1281 (1993).
24. J. Talbot, G. Tarjus, P. R. V. Tassel, P. Viot, From car parking to protein adsorption: An overview of sequential adsorption processes. *Colloids Surf. A Physicochem. Eng. Asp.* **165**, 287–324 (2000).
25. P. L. Krapivsky, S. Redner, E. Ben-Naim, *A Kinetic View of Statistical Physics* (Cambridge University Press, 2010).
26. J. D. Sherwood, Random sequential adsorption of lines and ellipses. *J. Phys. A Math. Gen.* **23**, 2827 (1990).
27. R. M. Ziff, R. D. Vigil, Kinetics and fractal properties of the random sequential adsorption of line segments. *J. Phys. A Math. Gen.* **23**, 5103 (1990).
28. G. Tarjus, P. Viot, Asymptotic results for the random sequential addition of unoriented objects. *Phys. Rev. Lett.* **67**, 1875 (1991).
29. D. Frenkel, B. Smit, *Understanding Molecular Simulation: From Algorithms to Applications* (Elsevier, 2001), vol. 1.
30. S. Torquato, F. H. Stillinger, Jammed hard-particle packings: From Kepler to Bernal and beyond. *Rev. Mod. Phys.* **82**, 2633 (2010).
31. H. N. W. Lekkerkerker, R. Tuinier, "Colloids and the depletion interaction" in *Lecture Notes in Physics* (Springer, ed. 2, 2024).
32. D. Frenkel, Order through entropy. *Nat. Mater.* **14**, 9–12 (2015).
33. K. Miyazaki, K. S. Schweizer, D. Thirumalai, R. Tuinier, E. Zaccarelli, The Asakura-Oosawa theory: Entropic forces in physics, biology, and soft matter. *J. Chem. Phys.* **156**, 080401 (2022).
34. P. Viot, G. Tarjus, S. M. Ricci, J. Talbot, Saturation coverage in random sequential adsorption of very elongated particles. *Phys. A Stat. Mech. Appl.* **191**, 248–252 (1992).
35. H. Edelsbrunner, D. Kirkpatrick, R. Seidel, On the shape of a set of points in the plane. *IEEE Trans. Inf. Theory* **29**, 551–559 (1983).
36. A. Rényi, Egy egydimenziós véletlen térkitöltési problémáról= on a one-dimensional problem concerning random space filling. *AMTK* **3**, 109–127 (1958).
37. H. Solomon, H. Weiner, A review of the packing problem. *Commun. Stat. Theory Methods* **15**, 2571–2607 (1986).
38. W. Krauth, *Statistical Mechanics: Algorithms and Computations* (OUP Oxford, 2006), vol. 13.
39. Y. Bhosale *et al*., Micromechanical origin of plasticity and hysteresis in nestlike packings. *Phys. Rev. Lett.* **128**, 198003 (2022).
40. O. B. Tsiok, V. V. Brazhkin, A. G. Lyapin, L. G. Khvostantsev, Logarithmic kinetics of the amorphous-amorphous transformations in SiO_2 and GeO_2 glasses under high pressure. *Phys. Rev. Lett.* **80**, 999 (1998).
41. E. R. Nowak, J. B. Knight, E. Ben-Naim, H. M. Jaeger, S. R. Nagel, Density fluctuations in vibrated granular materials. *Phys. Rev. E* **57**, 1971 (1998).
42. W. Götze, M. Sperl, Logarithmic relaxation in glass-forming systems. *Phys. Rev. E* **66**, 011405 (2002).
43. M. Nicodemi, A. Coniglio, H. J. Herrmann, The compaction in granular media and frustrated Ising models. *J. Phys. A Math. Gen.* **30**, L379 (1997).
44. E. Ben-Naim, J. B. Knight, E. R. Nowak, H. M. Jaeger, S. R. Nagel, Slow relaxation in granular compaction. *Phys. D Nonlinear Phenom.* **123**, 380–385 (1998).
45. M. Nicodemi, A. Coniglio, H. J. Herrmann, Frustration and slow dynamics of granular packings. *Phys. Rev. E* **55**, 3962 (1997).
46. F. Corberi, M. Nicodemi, M. Piccioni, A. Coniglio, Slow dynamics and aging in a constrained diffusion model. *Phys. Rev. E* **63**, 031106 (2001).
47. E. D. Gado, A. Fierro, L. de Arcangelis, A. Coniglio, Slow dynamics in gelation phenomena: From chemical gels to colloidal glasses. *Phys. Rev. E Stat. Nonlinear Soft Matter Phys.* **69**, 051103 (2004).
48. Y. Liu *et al*., A generative model of the connectome with dynamic axon growth. *Netw. Neurosci.* **8**, 1192–1211 (2024).
49. I. Bonamassa, Bundling_spaghetti. Github. https://github.com/hokanoei/Bundling_spaghetti. Deposited 21 July, 2025.